Numerical analysis of the axisymmetric lattice Boltzmann method for steady and oscillatory flows in periodic geometries

Samuel J. Stephen[1] Barbara M. Johnston[2]
Peter R. Johnston[3]

(Received 27 January 2023; revised 1 June 2024)

Abstract

Compared to more typical computational fluid dynamics techniques, the lattice Boltzmann method (LBM) is relatively new and unexplored. In recent years, axisymmetric LBM formulations, which can simulate flow in rotationally symmetric 3D geometries, have been published. Here we verify a novel axisymmetric LBM implementation using numerical criteria. Hagen–Poiseuille and Womersley flow are considered within a straight tube where analytic solutions are available. With this, we establish sufficient accuracy of the approximated flow and study the effects of changing simulation parameters (e.g. Reynolds number, Womersley number) and spatial/temporal parameters (e.g. relaxation

DOI:10.21914/anziamj.v64.17949, © Austral. Mathematical Soc. 2024. Published 2024-07-10, as part of the Proceedings of the 20th Biennial Computational Techniques and Applications Conference. ISSN 1445-8810. (Print two pages per sheet of paper.) Copies of this article must not be made otherwise available on the internet; instead link directly to the DOI for this article.

time, mesh nodes, time steps). Furthermore, steady and oscillatory flows within a periodically-varying, longitudinally asymmetric geometry are considered. Analytic solutions are not available in these cases; however, the validity of the axisymmetric LBM for curved boundaries is ensured through convergence, mesh independence and qualitative observations. Guaranteeing reasonable flow field determination for the aformentioned geometry is relevant to a larger problem where particulate suspension is pumped back and forth through a membrane of axisymmetric micropores. In these circumstances, experiments have induced directed particle transport even though there is no net flow of the carrier fluid. Hence, our work aims to improve current numerical simulations of these flow problems to better understand the factors that facilitate particle transport.

Contents

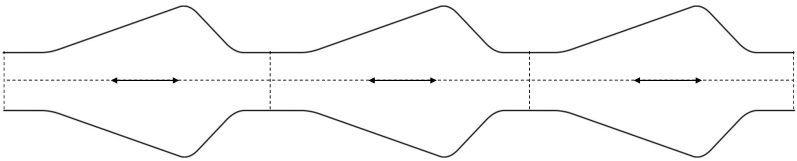

Figure 1: Axisymmetric, longitudinally asymmetric, periodic micropore cross-section.

1 Introduction

Modelling fluid flow within micropores can provide valuable insights across a wide range of applications [2]. A common issue that arises in problems with complex pore profiles is solution intractability. In recent years, there has been a resurgence of work aimed at a more comprehensive determination of the flow fields and suspended particle trajectories in axisymmetric micropore structures [4, 7]. A more specific problem considers a suspension that is pumped back and forth between two basins separated by a membrane consisting of many axisymmetric micropores. These micropores are spatially periodic and longitudinally asymmetric, with some configurations yielding directed particle movement from one basin to the other. Achieving suspended particle transport with no net flow of the carrier fluid is favourable as it bodes well for the system's applicability as a *Brownian motor* [1], which would be beneficial in the design of microfluidic devices. The curved sawtooth axisymmetric pore cross-section in Figure 1 is an example of the aforementioned micropore structures. An improved determination of the resulting flow fields would aid substantially in related research and development [4, 7].

Flow through axisymmetric micropores has been recently studied extensively utilising a boundary element method [3]. In those simulations, boundary integrals are required to obtain surface forces and Stokes flow is assumed in order to avoid inertial terms and to make the solution tractable. In contrast, one of the main advantages of the lattice Boltzmann method (LBM) is consistent boundary conditions that do not become more difficult to implement

as the geometry becomes more complex [6]. Also, periodic boundary conditions in the main flow direction are more straightforward to implement in the LBM. In addition, the LBM solves the Boltzmann equation which is equivalent to the Navier–Stokes equations through Chapman–Enskog analysis [6]. This means the Reynolds number (Re) can be freely set rather than applying the Stokes flow restriction of $\mathrm{Re} \ll 1$. In a previous study, we developed a novel axisymmetric LBM implementation, which was then able to simulate oscillatory fluid flow in longitudinally symmetric and asymmetric geometries [8]. Here, we aim to thoroughly study the convergence behaviour of that implementation.

2 Axisymmetric lattice Boltzmann method

2.1 Axisymmetric flow equations

Due to axisymmetry, we need only consider an axial direction z and radial direction r as part of a reduced 3D cylindrical coordinate system. Adopting the Einstein summation convention, the governing equations are [10]

$$\frac{\partial u_i}{\partial t} + u_j \frac{\partial u_i}{\partial x_j} = -\frac{1}{\rho}\frac{\partial p}{\partial x_i} + \nu \frac{\partial^2 u_i}{\partial x_j^2} + \frac{\nu}{r}\frac{\partial u_i}{\partial r} - \frac{\nu u_i}{r^2}\delta_{ir} \quad \text{and} \quad \frac{\partial u_j}{\partial x_j} = -\frac{u_r}{r}, \tag{1}$$

where $i, j \in \{z, r\}$, t is time, p is pressure, ρ is fluid density, ν is kinematic viscosity, x_i and x_j represent position, u_i and u_j are the velocity components and δ_{ir} is the Kronecker delta.

2.2 Formulation

The LBM evolves partial fluid densities on a lattice by incorporating a collision step and streaming step. The axisymmetric lattice Boltzmann equation takes the form [10]

$$f_\alpha(\mathbf{x} + \boldsymbol{e}_\alpha \Delta t, t + \Delta t) - f_\alpha(\mathbf{x}, t) = -\tau_\alpha(f_\alpha - f_\alpha^{eq}) + w_\alpha \theta \Delta t + \frac{\Delta t}{\kappa c^2} e_{\alpha i} F_i, \tag{2}$$

where f_α is the distribution function of particles, $\boldsymbol{x}$ is the position vector, t is time, α is a subscript to denote direction in the D2Q9 lattice velocity model (Figure 2), Δx is the lattice spacing, Δt is the time step, and $c = \Delta x/\Delta t$ is the lattice speed. The weighting according to the D2Q9 is

$$w_\alpha = (4/9, 1/9, 1/36, 1/9, 1/36, 1/9, 1/36, 1/9, 1/36)\,, \tag{3}$$

the lattice velocity is

$$\boldsymbol{e} = c((0,0),(1,0),(1,1),(0,1),(-1,1),(-1,0),(-1,-1),(0,-1),(1,-1))\,, \tag{4}$$

a constant is

$$\kappa = \frac{1}{c^2}\sum_\alpha e_{\alpha z} e_{\alpha z} = \frac{1}{c^2}\sum_\alpha e_{\alpha r} e_{\alpha r} = 6\,, \tag{5}$$

and some additional terms are

$$\theta = -\frac{\rho u_r}{r}\,, \quad \tau_\alpha = \frac{1}{2\tau}\left(2 + \frac{(2\tau-1)e_{\alpha r}\Delta t}{r}\right) \quad \text{and}$$
$$F_i = -\frac{\rho u_i u_r}{r} - \frac{2\rho\nu u_i}{r^2}\delta_{ir}\,, \quad i \in \{z, r\}\,, \tag{6}$$

where all terms containing r in the denominators are set to zero when $r = 0$ to avoid singularities [10]. The relaxation time τ describes the characteristic time a system away from equilibrium takes to relax to equilibrium. The local equilibrium distribution is defined as

$$f_\alpha^{eq} = w_\alpha \rho\left(1 + 3\frac{e_{\alpha r}u_r + e_{\alpha z}u_z}{c^2} + \frac{9}{2}\frac{(e_{\alpha r}u_r + e_{\alpha z}u_z)^2}{c^4} - \frac{3}{2}\frac{u_r^2 + u_z^2}{c^2}\right), \tag{7}$$

where u_r and u_z are the directional components of the macroscopic velocity and ρ is the fluid density. For every time step, conservation of mass and momentum require, respectively,

$$\rho = \sum_\alpha f_\alpha\,, \quad u_i = \frac{1}{\rho}\sum_\alpha e_{\alpha i} f_\alpha\,. \tag{8}$$

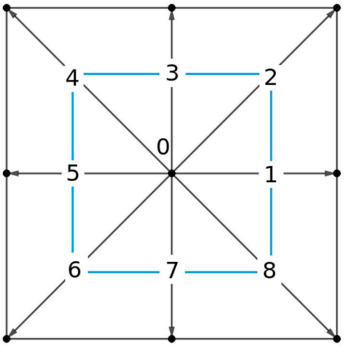

Figure 2: D2Q9 lattice velocity model.

Even though this axisymmetric LBM has been verified previously [9], here we provide an in-depth analysis discussing the effect of changing intrinsic parameters on the method's accuracy. The implementation used here is independently developed and thus validation is necessary.

2.3 Parameters

For characteristic length defined as twice the maximum radius R of the axisymmetric cross-section (Figure 1), the Reynolds number, Mach number and kinematic viscosity are [8], respectively,

$$\mathrm{Re} = \frac{2U_c R}{\nu}, \quad \mathrm{Ma} = \frac{\sqrt{3}U_c}{c} \quad \text{and} \quad \nu = \frac{c^2 \Delta t(2\tau - 1)}{6}, \tag{9}$$

where U_c is the characteristic velocity. It is essential to ensure $\mathrm{Ma} < 0.3$ to maintain reasonable accuracy [6]. Due to the underlying assumption of simulated fluids being Newtonian and incompressible, we require the numerical velocities to be sufficiently low so that compressible effects are circumvented.

To reliably achieve appropriate Mach numbers Ma across all simulations, the simple choice of $\Delta x = \Delta t = 1$ works well. Firstly, this sets the number of

radial nodes in the lattice to $N_r = R$ and the number of time steps to $N_t = T$ where T is the total time in the case of steady flow and the duration of the temporal period in the case of oscillatory flow. Setting the lattice spacing and time step like this also yields $U_c = \mathrm{Re}(2\tau - 1)/(12N_r)$. Then to achieve low Ma for any given τ and Re, the mesh resolution is increased.

2.4 Boundary conditions

In the computational domain, we consider a single spatial period. At the left ($z = 0$) and right ($z = L$) interfaces of the domain, the generalised periodic boundary condition is used [5]. This condition is highly efficient and works by streaming outbound partial densities to the opposite end to simulate indefinitely repeated geometries on each side.

There is an axisymmetry condition on the centreline ($r = 0$) which reflects the radial lattice velocities $\boldsymbol{e}$ of outbound densities while keeping the same axial lattice velocity. Variations of a no-slip condition are utilised for the upper hard wall boundary. A simple bounce-back condition is used for straight wall simulations where the lattice velocities of outbound densities are reflected in both directions, and the interpolated bounce-back condition [6] is used for the curved sawtooth geometry from Figure 1. Finally, a pressure gradient is the driving force of the flow. This is added to the axial component of the force term F_i from equation (6) and varies depending on the nature of the flow.

3 Steady flow

To achieve constant flow in the positive axial direction, the pressure gradient needs to be constant. To apply this, we add a constant pressure p_0 to the axial component of the force term from equation (6):

$$F_i = -\frac{\rho u_i u_r}{r} - \frac{2\rho\nu u_i}{r^2}\delta_{ir} + p_0\delta_{iz}\,, \quad i \in \{z, r\}\,. \tag{10}$$

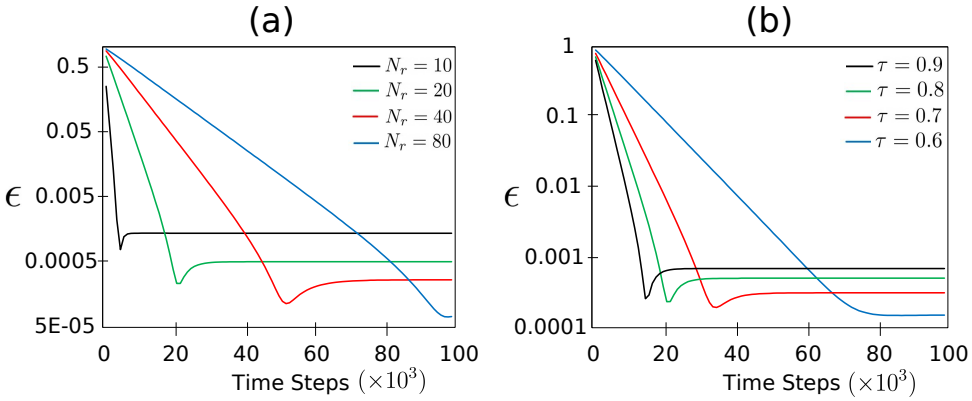

Figure 3: L2-norm error versus time steps for $Re = 1$ and (a) varying number of radial nodes N_r with $\tau = 0.8$; (b) varying relaxation times τ with $N_r = 40$.

3.1 Hagen–Poiseuille flow (steady flow in a pipe)

Hagen–Poiseuille flow is characterised as axisymmetric steady flow through a pipe with constant radius and length much larger than its radius. To quantify the effectiveness of our numerical simulations, the L2-norm error of the velocity is calculated via

$$\epsilon = \sqrt{\frac{\int_0^R [u_z(r) - u_{za}(r)]^2 \, dr}{\int_0^R u_{za}(r)^2 \, dr}} \quad \text{where} \quad u_{za}(r) = \frac{p_0}{4\nu\rho}(R^2 - r^2)\,. \tag{11}$$

Here u_z is the numerical axial velocity calculated through the LBM and u_{za} is the analytic parabolic axial velocity for Hagen–Poiseuille flow. The integrals in equation (11) are approximated with summations due to the LBM only obtaining velocities at discrete lattice positions. The benefit of starting with Hagen–Poiseuille flow is that an analytic solution is available because of the simple geometry. The density of the fluid can be set freely but the choice of $\rho = (p_0 R^2)/(4 U_c \nu)$ simplifies matters as the maximum velocity on the centreline $r = 0$ becomes the characteristic velocity U_c.

Figure 3 showcases two sets of numerical L2-norm error studies when using the

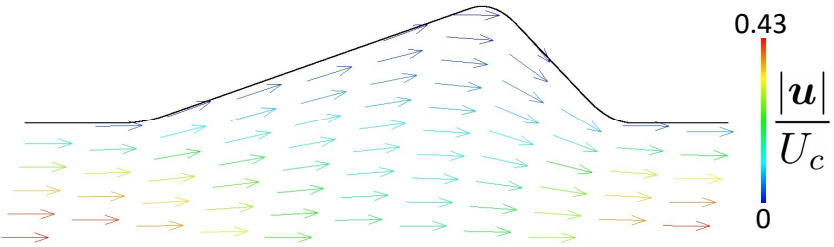

Figure 4: Velocity vector field of steady flow through asymmetric geometry.

axisymmetric LBM to calculate Hagen–Poiseuille flow. For simplicity, $\mathrm{Re} = 1$ across all simulations. For Figure 3(a), $\tau = 0.8$ when four different mesh resolutions are trialled, whereas $N_r = 40$ in Figure 3(b) for four simulations with varying τ. In both plots, the horizontal axis is in thousands of time steps and the vertical axis is a log scale of L2-norm error. Changing N_r and τ individually creates a trade-off between convergence and accuracy. From Figure 3(a), increasing the number of radial nodes N_r slows convergence but reduces error. Similarly, a lower value of τ corresponds to lower error solutions at the cost of slower convergence. The error tends to constant values in both plots as the numerical solutions converge.

3.2 Steady flow in an asymmetric geometry

We also simulate steady flow in pipes with variable radius. In particular, Figure 4 presents the macroscopic velocity vector field in the curved sawtooth profile, as calculated by the axisymmetric LBM. Only a subset of the vectors are visualised for clarity. Solutions were calculated with the axial length of one spatial period $L = 3R$, constriction of $R/2$ at inlet and outlet, $\mathrm{Re} = 1$, $N_r = 40$ and $\tau = 0.8$. The same simulation was conducted with different mesh resolutions and it was found that the velocity profile, when scaled by U_c, converged quickly, indicating mesh independence of the solution. The colour map given in Figure 4 highlights areas of high velocity with red and low velocity with blue. The axial velocity profile in the constriction regions ($z = 0$

and $z = 3R$) resembles Hagen–Poiseuille flow solutions whereas the axial velocity profile at the maximum expansion ($z = 2R$) flattens as $r/R \to 1$ with non-zero radial velocity contributions in the main channel and expansion region.

4 Oscillatory flow

To achieve oscillating flow, the pressure gradient term needs to be sinusoidal instead of constant. Therefore, the force term is altered to

$$F_i = -\frac{\rho u_i u_r}{r} - \frac{2\rho\nu u_i}{r^2}\delta_{ir} + p_0 \cos\left(\frac{2\pi t}{T}\right)\delta_{iz}\,, \quad i \in \{z, r\}\,, \tag{12}$$

where p_0 is the maximum amplitude of pressure and T is the period of the oscillation. This time-varying addition gives rise to a dimensionless parameter, the Womersley number

$$W_0 = R\sqrt{\frac{2\pi}{T\nu}}\,, \quad \text{giving} \quad N_t = \frac{12\pi N_r^2}{{W_0}^2(2\tau - 1)}\,. \tag{13}$$

The number of time steps N_t is inversely proportional to W_0^2, which means that lower Womersley numbers require more time steps to calculate flow fields.

4.1 Womersley flow (oscillatory flow in a pipe)

Womersley flow is characterised as flow in a long straight pipe with temporally periodic pressure variations. Once again, the simplified geometry means we have access to an analytic solution given by [10]

$$u_{za}(r, t) = \Re\left[\frac{p_0 T}{2\pi i\rho}\left(1 - \frac{J_0(r\phi/R)}{J_0(\phi)}\right)e^{2\pi i t/T}\right], \tag{14}$$

where J_0 is the zeroth-order Bessel function of the first kind and $\phi = W_0(-1+i)/2$.

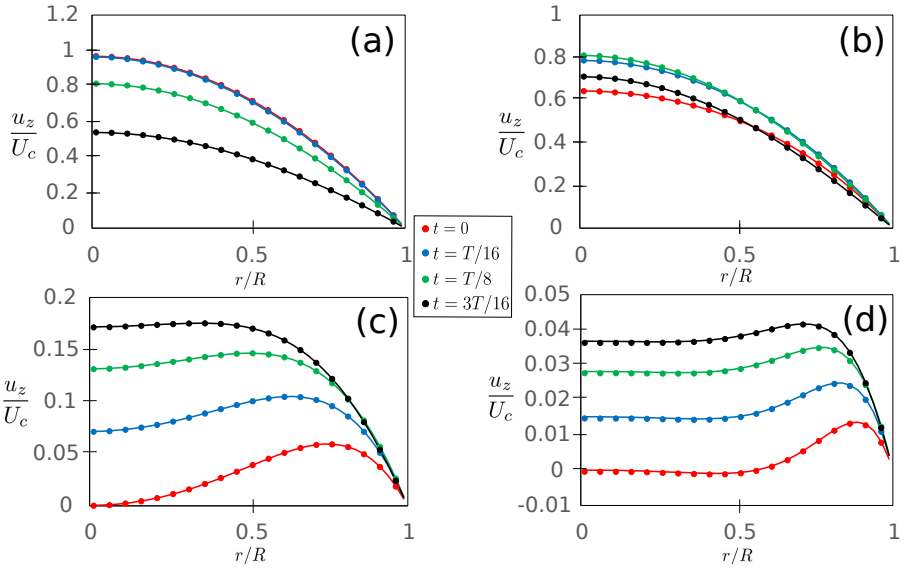

Figure 5: Comparison of flows with different Womersley numbers (a) $W_0 = 1$; (b) $W_0 = 2$; (c) $W_0 = 5$; (d) $W_0 = 10$. Dots represent the numerical velocities whereas lines represent the analytic solutions.

Figure 5 plots the axial velocity profiles against radial position for four values of W_0, each at four time points within the first quarter of the period. For these simulations, the parameters are set to $\mathrm{Re} = 1$, $\tau = 0.75$ and $N_r = 40$. Figure 5(a) shows the velocities for $W_0 = 1$, where a parabolic profile emerges with decreasing maximum velocity as time passes. This is expected as the pressure term in equation (12) is at its maximum positive value at $t = 0$. As $t \to T/4$, the pressure drops causing a decrease in velocity. Lower values of W_0 correspond to a velocity flow profile that is more sensitive to pressure changes. On the other end of the spectrum, the higher value of $W_0 = 10$ produces a velocity profile reminiscent of plug flow, which is much less responsive to pressure changes and exhibits slower speeds overall.

All numerical velocities presented in Figure 5 agree nicely with the analytic

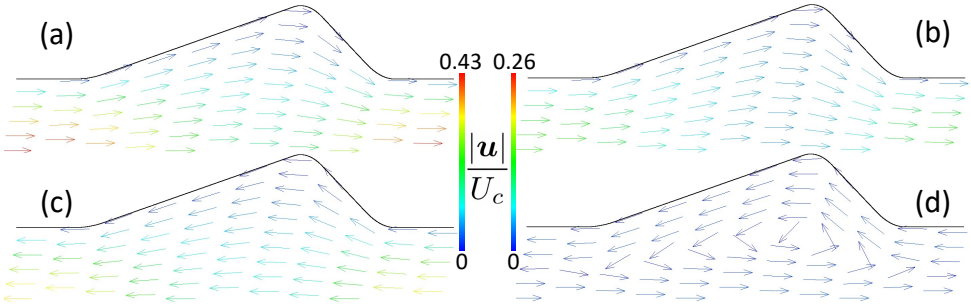

Figure 6: Velocity vector fields of oscillatory flow through asymmetric geometry with (a) $t/T = 0$, $W_0 = 1$; (b) $t/T = 0$, $W_0 = 5$; (c) $t/T = 0.4$, $W_0 = 1$; (d) $t/T = 0.4$, $W_0 = 5$.

solutions; however, the axial velocity L2-norm error throughout the period is $\epsilon \approx 10^{-2}$ for $W_0 = 10$, whereas $\epsilon \approx 10^{-3}$ for a lower value of W_0. This is unsurprising, as higher values of W_0 require fewer time steps for the same parameter set from equation (13).

4.2 Oscillatory flow in an asymmetric geometry

Having established sufficient accuracy and convergence of the axisymmetric LBM implementation with preliminary simulations, we now arrive at the desired simulation. Here we keep all characteristics of Womersley flow and change the pore boundary to that of the longitudinally asymmetric curved sawtooth profile. Figure 6 depicts velocity vector fields at two time points, with $W_0 = 1$ and $W_0 = 5$.

Immediately we observe that Figure 6(a) resembles the steady-state flow field from Figure 4, whereas the velocity in Figure 6(b) is slower and more uniform in magnitude across the main channel, as expected. This is similar to the differences seen in Figure 5(a) and Figure 5(c). Another major observation is that the flow field for $W_0 = 5$ is still reversing at $t/T = 0.4$ (Figure 6(d)), while for $W_0 = 1$ it has reversed entirely (Figure 6(c)). These

observations demonstrate the similarities with expected fluid behaviours from the Womersley flow results (Figure 5) which adds to the credibility of these solutions.

5 Conclusion

In summary, we presented multiple simulations for various flow problems and parameters leading up to oscillatory fluid flow through an axisymmetric, longitudinally asymmetric and spatially periodic micropore structure. The importance of three key parameters was investigated throughout. Increasing mesh resolution and lowering relaxation time resulted in higher accuracy at the cost of slower convergence. Additionally, lowering the Womersley number produces less error overall; however, the number of time steps required increases rapidly. This is potentially problematic for simulations with typical nanoscale conditions such as low Reynolds and Womersley numbers. Nevertheless, the main goal of verifying the independently developed axisymmetric LBM implementation was achieved. Thus, this method of flow field determination is reliable and can be coupled with a suspended particle transport solver in future work.

References

[1] R. D. Astumian and P. Hänggi. "Brownian motors". In: *Phys. Today* 55.11 (2002), pp. 33–39. DOI: 10.1063/1.1535005. (Cit. on p. C214).

[2] W. R. Bowen and F. Jenner. "Theoretical descriptions of membrane filtration of colloids and fine particles: An assessment and review". In: *Adv. Colloid Interface Sci.* 56 (1995), pp. 141–200. DOI: 10.1016/0001-8686(94)00232-2 (cit. on p. C214).

[3] N. Islam. "Fluid flow and particle transport through periodic capillaries". In: *Bull. Aust. Math. Soc.* 96.3 (2017), pp. 521–522. DOI: 10.1017/S0004972717000739 (cit. on p. C214).

[4] C. Kettner, P. Reimann, P. Hänggi, and F. Müller. "Drift ratchet". In: *Phys. Rev. E* 61.1 (2000), pp. 312–323. DOI: 10.1103/PhysRevE.61.312 (cit. on p. C214).

[5] S. H. Kim and H. Pitsch. "A generalized periodic boundary condition for lattice Boltzmann method simulation of a pressure driven flow in a periodic geometry". In: *Phys. Fluids* 19.10, 108101 (2007). DOI: 10.1063/1.2780194 (cit. on p. C218).

[6] T. Krüger, H. Kusumaatmaja, A. Kuzmin, O. Shardt, G. Silva, and E. M. Viggen. *The lattice Boltzmann method: Principles and practice*. Vol. 10. Graduate Texts in Physics. Springer, 2017, pp. 978–3. DOI: 10.1007/978-3-319-44649-3 (cit. on pp. C215, C217, C218).

[7] S. Matthias and F. Müller. "Asymmetric pores in a silicon membrane acting as massively parallel brownian ratchets". In: *Nature* 424 (2003), pp. 53–57. DOI: 10.1038/nature01736 (cit. on p. C214).

[8] S. J. Stephen, B. M. Johnston, and P. R. Johnston. "Comparing lattice Boltzmann simulations of periodic fluid flow in repeated micropore structures with longitudinal symmetry and asymmetry". In: *Proceedings of the 15th Biennial Engineering Mathematics and Applications Conference, EMAC-2021*. Ed. by A. Clark, Z. Jovanoski, and J. Bunder. Vol. 63. ANZIAM J. 2022, pp. C69–C83. DOI: 10.21914/anziamj.v63.17158 (cit. on pp. C215, C217).

[9] W. Wang and J. Zhou. "Enhanced Lattice Boltzmann modelling of axisymmetric flows". In: *Proceedings of the Institution of Civil Engineers—Engineering and Computational Mechanics* 167.4 (2014), pp. 156–166. DOI: 10.1680/eacm.14.00005 (cit. on p. C217).

[10] J. G. Zhou. "Axisymmetric lattice Boltzmann method revised". In: *Phys. Rev. E* 84.3, 036704 (2011). DOI: 10.1103/PhysRevE.84.036704 (cit. on pp. C215, C216, C221).

Author addresses

1. **Samuel J. Stephen**, Queensland Micro- and Nanotechnology Centre, Griffith University, Nathan, Queensland 4111, AUSTRALIA.
mailto:samuel.stephen@griffith.edu.au
orcid:0000-0003-2884-2923

2. **Barbara M. Johnston**, School of Environment and Science, Griffith University, Nathan, Queensland 4111, AUSTRALIA.

3. **Peter R. Johnston**, School of Environment and Science, Griffith University, Nathan, Queensland 4111, AUSTRALIA.